Corrosion Science 167 (2020) 108479

Contents lists available at ScienceDirect

Corrosion Science

journal homepage: www.elsevier.com/locate/corsci

Effects of nanosized TiC and TiB_2 particles on the corrosion behavior of Al-Mg-Si alloy

Run Geng[a,b], Si-Qi Jia[b], Feng Qiu[a,b], Qing-Long Zhao[a,b,*], Qi-Chuan Jiang[a,b,*]

[a] State Key Laboratory of Automotive Simulation and Control, Jilin University, PR China
[b] Key Laboratory of Automobile Materials, Ministry of Education and School of Materials Science and Engineering, Jilin University, No. 5988 Renmin Street, Changchun 130025, PR China

ARTICLE INFO

Keywords:
Aluminum
XPS
TEM
Intergranular corrosion
Passive films

ABSTRACT

Nanosized TiC and TiB_2 particles (TiC_p, TiB_{2p}) can increase the mechanical properties of Al alloys. However, their effects on the corrosion performance of Al alloys are relatively less understood. The corrosion behavior of Al-Mg-Si alloys is improved by adding TiC_p and worsened by adding TiB_{2p}. These changes result from i. TiC_p refining the grain structure by acting as nucleants and reducing the number of grain boundary phases and ii. TiB_{2p} segregating at grain boundaries and accelerating the corrosion. This provides a selection criterion that can be utilized for reinforcement nanoparticles for wrought Al alloys that are applied in corrosive environments.

1. Introduction

Inoculants such as Al-Ti-C and Al-Ti-B have been widely applied in the industrial production of Al alloys to obtain the grain refinement [1,2]. Generally, micron-sized TiC and TiB_2 can act as heterogeneous nucleation sites during solidification, leading to the grain refinement of Al alloys [3]. Grain refinement could improve the mechanical properties of Al alloys based on the well-known Hall-Petch relation. When the TiC and TiB_2 are added as reinforcement nanoparticles, they can also improve the mechanical properties based on the Orowan mechanism. Nanoparticles can refine grains more efficiently and simultaneously increase the strength and ductility in contrast with the micron-sized particles [4]. Recently, nanosized TiC_p were introduced into an Al-Mg-Si alloy as reinforcement particles, and the tensile strength increased significantly [5]. It also has been proved that nanoparticles can improve the creep properties and the wear resistance of Al alloys [6–9]. It has been reported that an increasing content of the micron-sized Al_2O_3 particles can cause decreased corrosion resistance [10]. In corrosive environments, the corrosion behavior becomes important, especially for Al-Mg-Si alloys used as structural materials in the marine and automotive industries. They are generally resistant to corrosion, but the presence of Mg_2Si and excess Si at grain boundaries introduce susceptibility to intergranular corrosion (IGC) [11]. Susceptibility to IGC relates to the formation of micro galvanic couplings by grain boundary phases [12,13]. The thermomechanical treatment and alloying, which are the usual ways to improve the mechanical properties, may increase the number of grain boundary phases [11,14]. The alloying process is usually performed to improve the strength of Al-Mg-Si alloys by adding Cu [15–17]. However, the IGC susceptibility of Al-Mg-Si alloys increases with the Cu content and excessive Si. In general, the improved mechanical properties of aluminum alloys obtained by alloying may cause decreased corrosion resistance because of the grain boundary phases. The simultaneous improvement of mechanical properties and corrosion resistance of Al-Mg-Si alloys is a challenge.

The addition of nanoparticles can effectively refine the grain structure during solidification and refine recrystallized grains during the heat treatment, leading to a more uniform grain structure [5,18]. Ralston and Birbilis reviewed the impact of grain size on corrosion performance [19]. It has been proposed that alloys can show an increase or decrease in corrosion resistance with grain refinement, depending on the ability of the environment to passivate. In an active environment, the grain refinement shows a negative effect on corrosion resistance while in an environment encouraging passivity, the grain refinement shows a positive effect on corrosion resistance. For Al alloys, many studies have proposed that a refined grain size could reduce the corrosion susceptibility [20–22]. In addition, if the same Al alloys possess the same average grain size, a narrow grain size distribution will be more corrosion resistant than a broader grain size distribution in a passive environment [23]. Therefore, the improved grain structure caused by nanoparticles is expected to improve the corrosion behavior of the Al-Mg-Si alloys. However, the corrosion properties of Al alloys after the addition of nanoparticles are relatively less well understood.

* Corresponding authors at: State Key Laboratory of Automotive Simulation and Control, Jilin University, PR China.
E-mail addresses: zhaoqinglong@jlu.edu.cn (Q.-L. Zhao), jqc@jlu.edu.cn (Q.-C. Jiang).

https://doi.org/10.1016/j.corsci.2020.108479
Received 2 September 2019; Received in revised form 17 December 2019; Accepted 16 January 2020
Available online 18 January 2020
0010-938X/

In this work, Al-Mg-Si alloys (AA6061) containing nanosized TiC_p and nanosized TiB_{2p} were evaluated by immersing into an accelerated corrosion solution and a 3.5 wt% NaCl solution, aiming to investigate the different corrosion behaviors after the addition of different nanoparticles. Furthermore, scanning electron microscopy (SEM) and transmission electron microscopy (TEM) were adopted to characterize the corrosion surfaces of samples and the grain boundary phases. Electrochemical and XPS measurements were taken to understand the corrosion behavior during the corrosion process. This paper aims to reveal the effects of nanosized TiC_p and TiB_{2p} on the corrosion behavior of Al-Mg-Si alloys to provide a selection criterion for reinforcement nanoparticles in wrought Al alloys.

2. Materials and methods

2.1. Materials and processing

In this paper, nanosized TiC_p and TiB_{2p} were fabricated by the self-propagation high-temperature synthesis (SHS) reactions of the Al-Ti-C system and Al-Ti-B systems, respectively. Thus, two kinds of powder mixtures were prepared to produce the TiC_p-Al and TiB_{2p}-Al master alloys: i. 70Al-Ti-carbon nanotubes (in wt%) with a Ti/C molar ratio of 1/1and ii. 80Al-Ti-B (in wt%) with a Ti/B molar ratio of 1/2. The powder mixtures were ball milled for 48 h at 50 rpm and then cold-pressed into cylindrical compacts with the same size: 40 mm × 28 mm (diameter × height). Finally, the compacts were heated to 1173 K in a vacuum thermal explosion furnace to ignite the SHS reactions and then cooled to room temperature. The nanosized TiC_p and TiB_{2p} were extracted from the master alloy using an 18 vol% HCl aqueous solution. The morphologies and the size statistics of TiC_p and TiB_{2p} are shown in Fig. 1. The TiC_p showed a spherical morphology with a mean diameter of 88 nm. The TiB_{2p} showed a prismatic morphology with a mean diameter of 140 nm.

The nominal compositions of the matrix 6061 Al alloy are as follows (in wt%): 0.87 % Mg, 0.55 % Si, 0.59 % Fe, 0.36 % Cu, 0.15 % Mn, 0.17 % Cr, 0.23 % Zn, 0.16 % Ti and balanced Al. The TiC_p-Al and TiB_{2p}-Al master alloys were introduced into the molten 6061 Al alloy at 1173 K. Mechanical stirring was carried out for 2 min after adding the master alloys to disperse the nanoparticles. The additions of the nanosized TiC_p and nanosized TiB_{2p} were both 0.5 wt%. Finally, the melts were cooled to 1073 K and poured into a preheated steel mold (200 × 50 × 20 mm^3). Homogenization was performed with the as-cast samples of the matrix alloy, the 0.5 wt% TiC_p/6061 Al composite (0.5-TiC_p) and the 0.5 wt% TiB_{2p}/6061 Al composite (0.5-TiB_{2p}) at 570 °C for 7 h.

The rolling samples were cut from the bottom of the homogenization treated castings using a wire-cut electrical discharge machine. The rolling samples were cold rolled from 6 mm to 1.8 mm with 5 rolling passes (four 1 mm passes and one 0.2 mm pass) followed by T6 heat treatment (holding the solution at 525 °C for 1 h and then aging at 180 °C for 5 h).

2.2. Accelerated corrosion test

Corrosion testing was performed according to the accelerated corrosion standard [14,24,25]. The standard involves the following steps: degreasing in ethanol, 5 min of etching in a 10 wt% NaOH solution at room temperature, 2 min of desmutting in a 30 wt% HNO_3 solution, and 24 h of immersion in an acidified sodium chloride solution (30 g of NaCl and 10 mL of HCl per liter). The test samples were 10 mm × 10 mm × 2 mm (Fig. 2) pieces cut from the rolling samples.

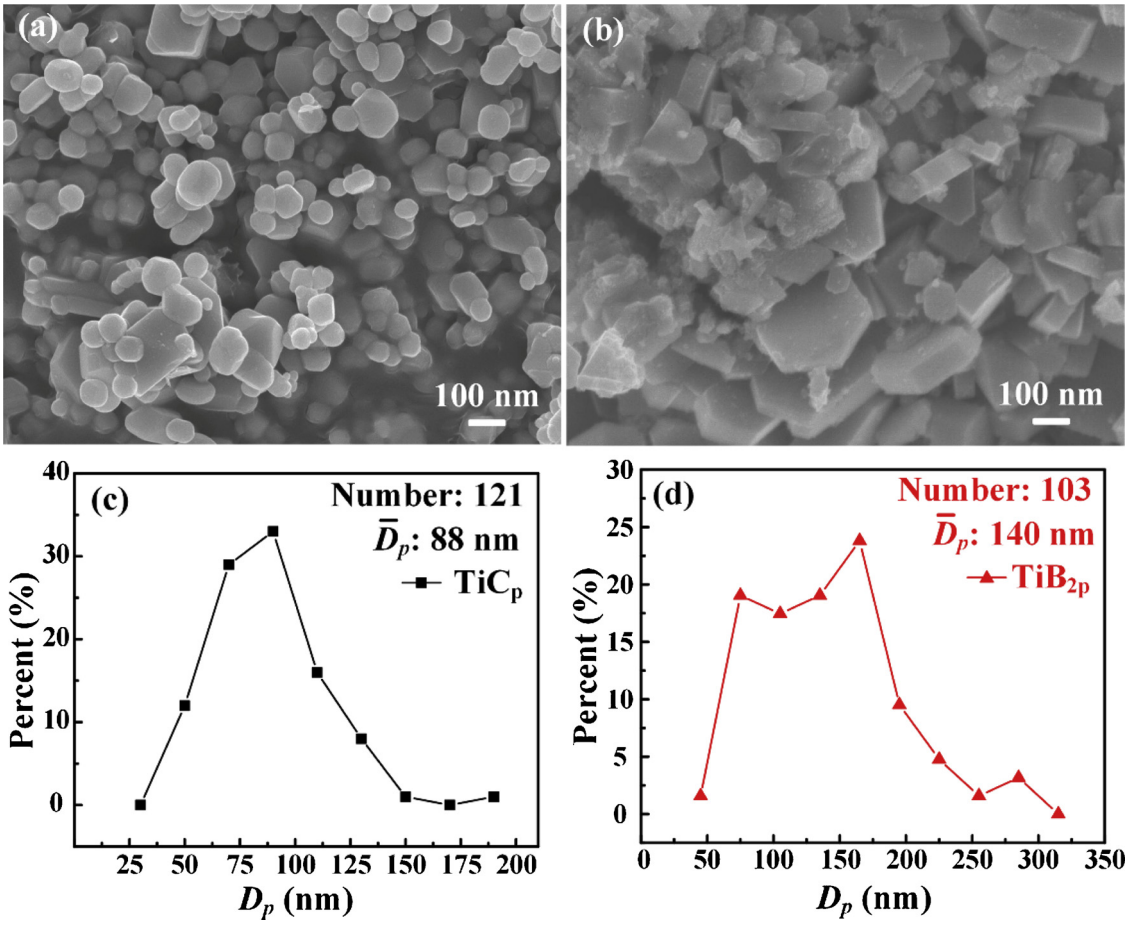

Fig. 1. Images of the nanosized (a) TiC_p and (b) TiB_{2p} extracted from the master alloy, and the size distribution diagrams of the (c) TiC_p and (d) TiB_{2p}.

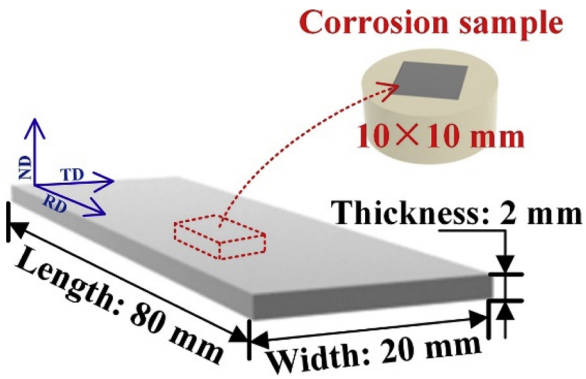

Fig. 2. Schematic drawing of the corrosion test sample.

Three specimens were prepared for each alloy. Before the corrosion test, the surfaces of the samples, except for the investigated surface, were covered by an epoxy resin. The solution volumes were adjusted to obtain a constant surface/solution ratio of 1 cm^2:12.5 ml. After immersion, the samples were washed in distilled water and then in ethanol. The morphology and corrosion depth were assessed by examining the entire (short-transverse) cross-sections using a scanning electron microscope (SEM) (Tescan vega3 XM, Czech Republic).

2.3. Immersing corrosion test

The samples for this test were the same as the samples in the accelerated corrosion test (10 mm × 10 mm × 2 mm). Before the corrosion test, the surfaces of the samples, except for the investigated surface, were covered by denture acrylic and polished mechanically with 5000-grid SiC emery paper. A 3.5 wt% NaCl solution was used in this test and changed every 24 h.

2.4. Electrochemical measurements

Electrochemical tests were performed in a 3.5 wt% NaCl solution (pH 6.8) at 27 °C on an electrochemical workstation (Versa STAT 4, Princeton Applied Research, USA). The electrolyte was purged with nitrogen gas for at least 30 min prior to each electrochemical test. A platinum mesh auxiliary electrode and a saturated calomel electrode (SCE + 0.242 V vs. SHE) were used as reference electrodes and were evaluated with an Electrochemical Analyzer (Versa STAT 4, Princeton Applied Research, USA). The tested alloys acted as working electrodes, and the work area was 1.0 cm^2. Before testing, all the specimens were mechanically polished and ultrasonically cleaned in ethanol. The electrochemical impedance spectroscopy (EIS) test parameters were as follows: the AC signal voltage amplitude was 5 mV, and the scan frequency was 0.01 − 100 kHz at open circuit potential (OCP) value. The OCP was recorded for ~ 600 s prior to polarization testing in order to establish an approximately stable potential. A Potentiodynamic polarization (PDP) test was carried out at a scanning rate of 1 mV/s and the

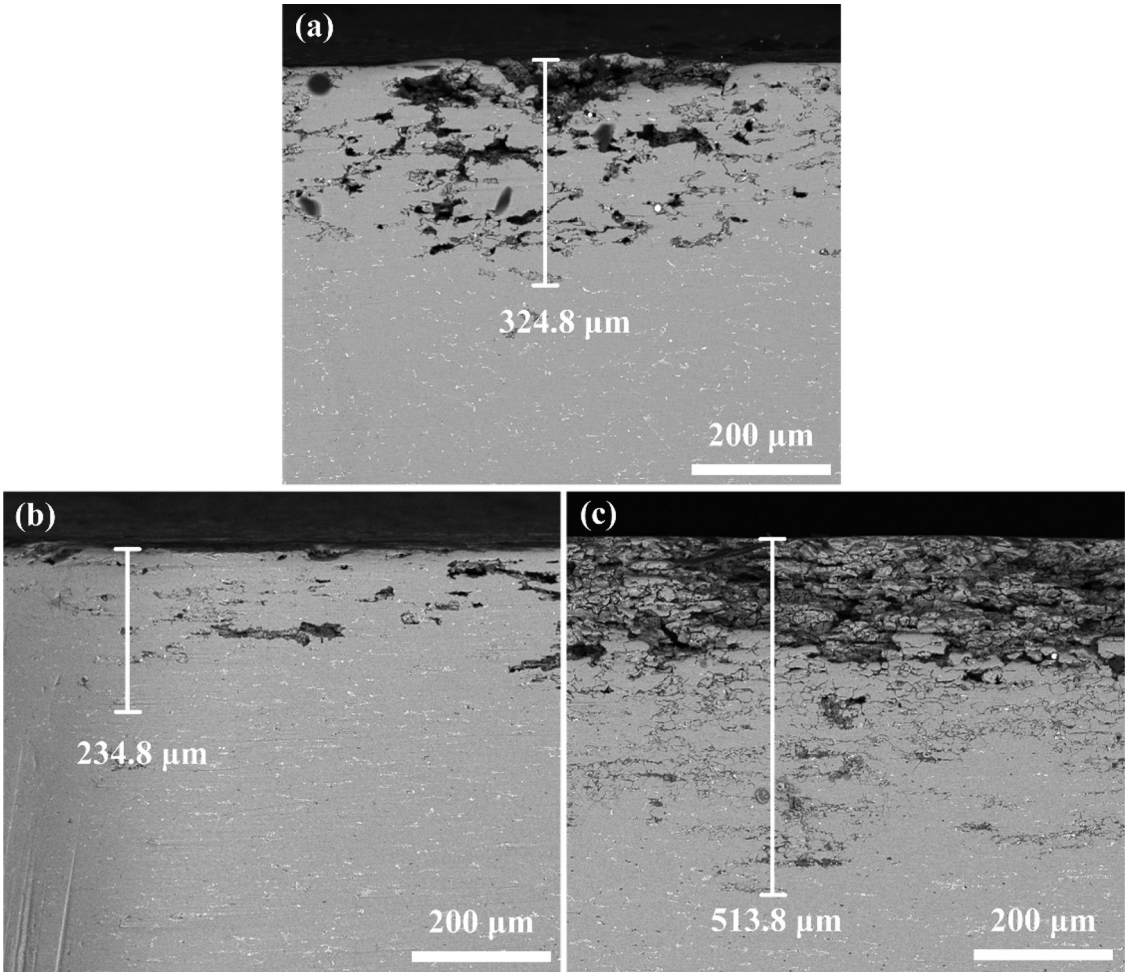

Fig. 3. Short-transverse sectional images of the samples after the accelerated corrosion test at room temperature: (a) the matrix alloy, (b) the 0.5-TiC_p composite, (c) the 0.5-TiB_{2p} composite.

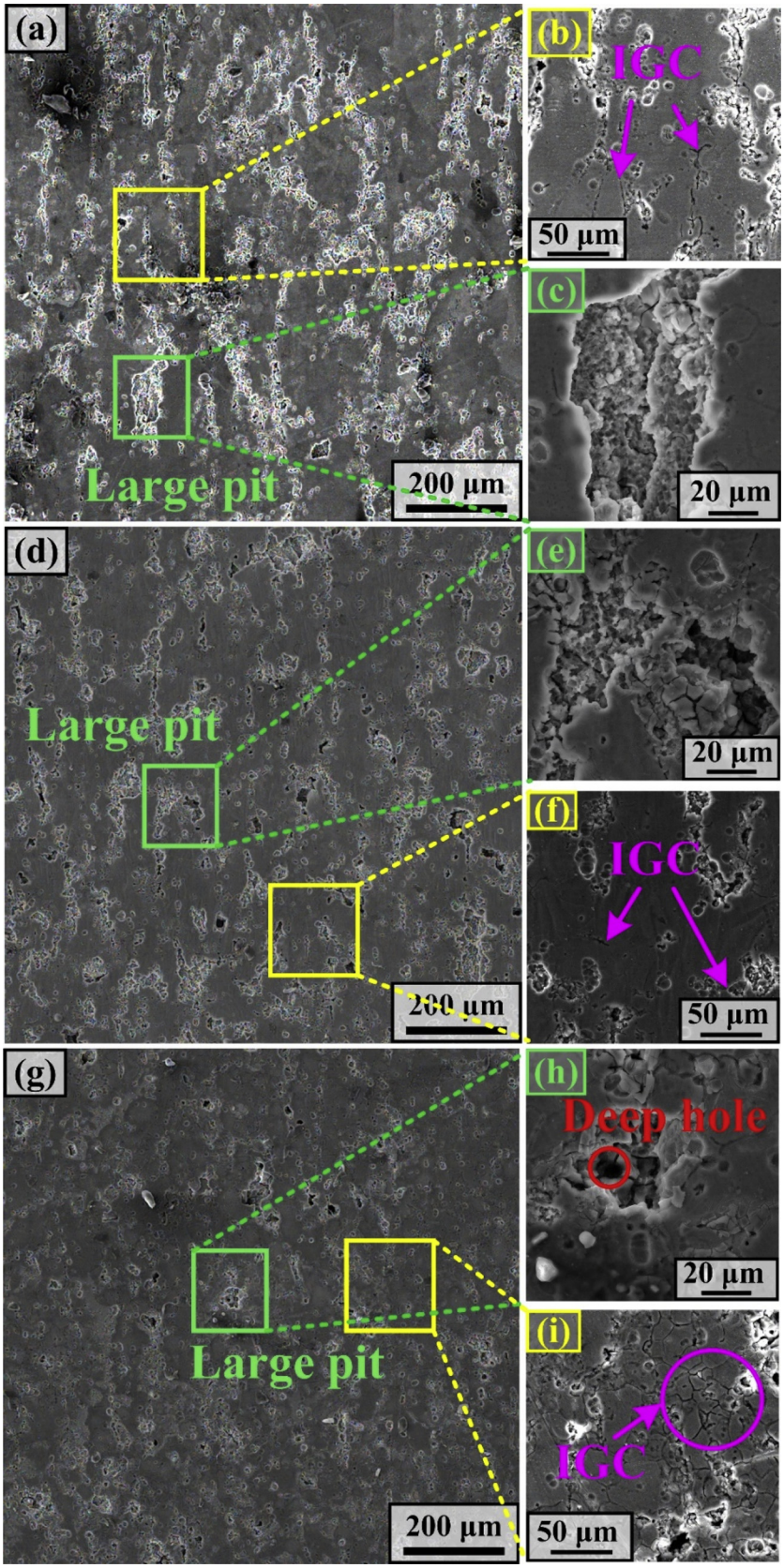

Fig. 4. Surface morphologies of the sample surfaces after the accelerated corrosion test: (a)-(c) the matrix alloy, (d)-(f) the 0.5-TiC_p composite and (g)-(i) the 0.5-TiB_{2p} composite.

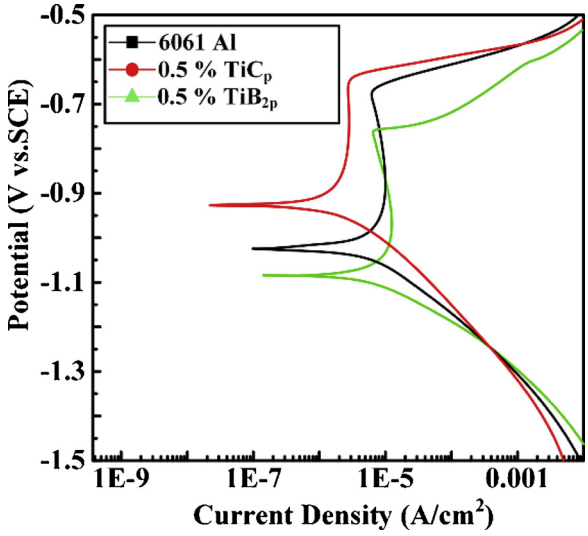

Fig. 5. The potentiodynamic polarization curves of the three investigated materials in the 3.5 wt% NaCl solution at room temperature.

Table 1
Polarization characteristics of the matrix alloy and the composites with different nanoparticles in the 3.5 wt.% NaCl solution.

	Corrosion potential E_{corr} vs.SCE (V)	Pitting potential E_{pit} vs.SCE (V)	Corrosion current density i_{corr} (μA/cm^2)
6061 Al	−1.027	−0.662	8.26
0.5 wt% TiC_p/6061	−0.927	−0.612	2.60
0.5 wt% TiB_{2p}/6061	−1.080	−0.750	9.06

potential was ramped from -1.0 V (vs. OCP) to +0.8 V. The corrosion current density (i_{corr}) and corrosion potentials (E_{corr}) were determined by the Tafel extrapolation method with the aid of the CorrView software. EIS measurements were carried out on the same sample after immersing in the 3.5 wt% NaCl solution for different times.

2.5. X-ray photoelectron spectroscopy measurements

X-ray photoelectron spectroscopy (XPS) measurements for surface analysis of the specimens immersed in the solution of the accelerated corrosion test were performed using a Thermo ESCALAB 250 photoelectron spectrometer with Al K_α excitation. The samples used in the XPS measurements were the same samples mentioned in Section 2.2, and all samples were immersed in absolute ethyl alcohol before the XPS measurements.

2.6. Microstructural analysis

The microstructures were observed using a SEM (Tescan vega3 XM). Transmission electron microscopy (TEM) (JEM-2100 F) was also used to characterize the microstructures. TEM thin foils were prepared using twin-jet electropolishing at −20 °C with a solution of 90 vol.% ethanol and 10 vol.% perchloric acid at 20 V.

3. Results

3.1. Corrosion behaviors

3.1.1. Accelerated corrosion tests

Fig. 3 shows the cross-sectional accelerated corroded morphologies of the matrix alloy, the 0.5-TiC_p composite and the 0.5-TiB_{2p} composite at room temperature. These samples were evaluated by the accelerated IGC test. The maximum corrosion depth (MCD) indicated the IGC susceptibility of the corroded alloys (Fig. 3). The MCD values of the matrix alloy, the 0.5-TiC_p composite, and the 0.5-TiB_{2p} composite were 324.8 μm, 234.8 μm and 513.8 μm, respectively. The matrix alloy was susceptible to pitting, as characterized by more localized attacks (Fig. 3(a)). The pitting was smaller in the 0.5-TiC_p composite (Fig. 3(b)). The 0.5-TiB_{2p} composite possessed a uniform network-sharped IGC (Fig. 3(c)–(d)).

Fig. 4 shows the accelerated corrosion surfaces of the matrix alloy, the 0.5-TiC_p composite, and the 0.5-TiB_{2p} composite. The corrosion pits and IGC were observed in the matrix alloy (Fig. 4(a–c)). Despite the presence of corrosion pits, the length of the IGC creak was reduced in the 0.5-TiC_p composite, compared to the matrix alloy (Fig. 4(d–f)). However, the 0.5-TiB_{2p} composite showed deep corrosion holes and severe IGC, compared to the matrix alloy and the 0.5-TiC_p composite (Fig. 4(g–i)). Thus, the 0.5-TiC_p composite showed the best corrosion behavior in the accelerated corrosion test.

3.1.2. Electrochemical measurements

The potentiodynamic polarization curves, tested in the 3.5 wt% NaCl solution, are shown in Fig. 5. The values of the corrosion potential (E_{corr}), pitting potential (E_{pit}) and corrosion current density (i_{corr}) can be derived from the potentiodynamic polarization curves, as summarized in Table 1. The E_{corr} values of the matrix alloy, the 0.5-TiC_p composite, and the 0.5-TiB_{2p} composite were -1.027 V, -0.927 V and -1.080 V, respectively, indicating that the corrosion tendency was reduced after adding the nanosized TiC_p and increased after adding the TiB_{2p}. All the curves showed a distinct pitting potential (E_{pit}), at which the current sharply increased. The E_{pit} values of the matrix alloy, the 0.5-TiC_p composite, and the 0.5-TiB_{2p} composite were -0.662 V, -0.612 V and -0.750 V, respectively, indicating that the pitting resistance of the 0.5-TiC_p composite improved, and that of the 0.5-TiB_{2p} composite became worse. The i_{corr} values of the matrix alloy, the 0.5-TiC_p composite, and the 0.5-TiB_{2p} composite were 8.26 μA/cm^2, 2.60 μA/cm^2 and 9.06 μA/cm^2, respectively. This indicated that the i_{corr} was decreased by the addition of TiC_p. Though the i_{corr} increased slightly after adding TiB_{2p}, the values of i_{corr} in the matrix alloy and the 0.5-TiB_{2p} composite were close.

To further investigate the corrosion process, EIS plots were recorded in the 3.5 wt% NaCl solution after immersing in the tested solution for different times (Fig. 6). The shape and size of the respective plots are different (Fig. 6). The larger diameter of the capacitive semicircle implies a better corrosion resistance [26]. As shown in Fig. 6(a), The decreasing diameters of capacitive loops indicated that the corrosion resistance decreased with time in the matrix alloy. The diameters of the capacitive loops in the 0.5-TiC_p composite increased after immersing for 6 h and subsequently decreased (Fig. 6(b)). This indicated that the corrosion resistance of the 0.5-TiC_p composite was increased firstly, then decreasing with time. The diameters of the capacitive loops in the 0.5-TiB_{2p} composite showed a similar decreasing trend with those of the matrix alloy (Fig. 6(c)). The decreasing diameters of capacitive loops indicated that the corrosion resistance decreased with time in the 0.5-TiB_{2p} composite. Meanwhile, the corrosion resistance of the matrix alloy and the 0.5-TiB_{2p} composite decreased a lot after immersing for 6 h. Thus, the 0.5-TiC_p composite showed an improved corrosion resistance, compared to the matrix alloy and the 0.5-TiB_{2p} composite, which corresponds to the result of i_{corr}.

3.1.3. XPS measurements

Figs. 7 and 8 show the spectrums of Al 2p and O 1s in these materials, respectively. The Al 2p spectrum of these materials can be deconvoluted into two characteristic peaks of Al metal (~ 72.6 eV) and Al oxide (~ 74.6 eV) [27]. The O 1s spectrum of these materials can be deconvoluted into two characteristic peaks of surface-adsorbed oxygen (~ 532.6 eV, O1) and oxygen in Al_2O_3 (~ 531.1 eV, O2) [28]. Thus, all

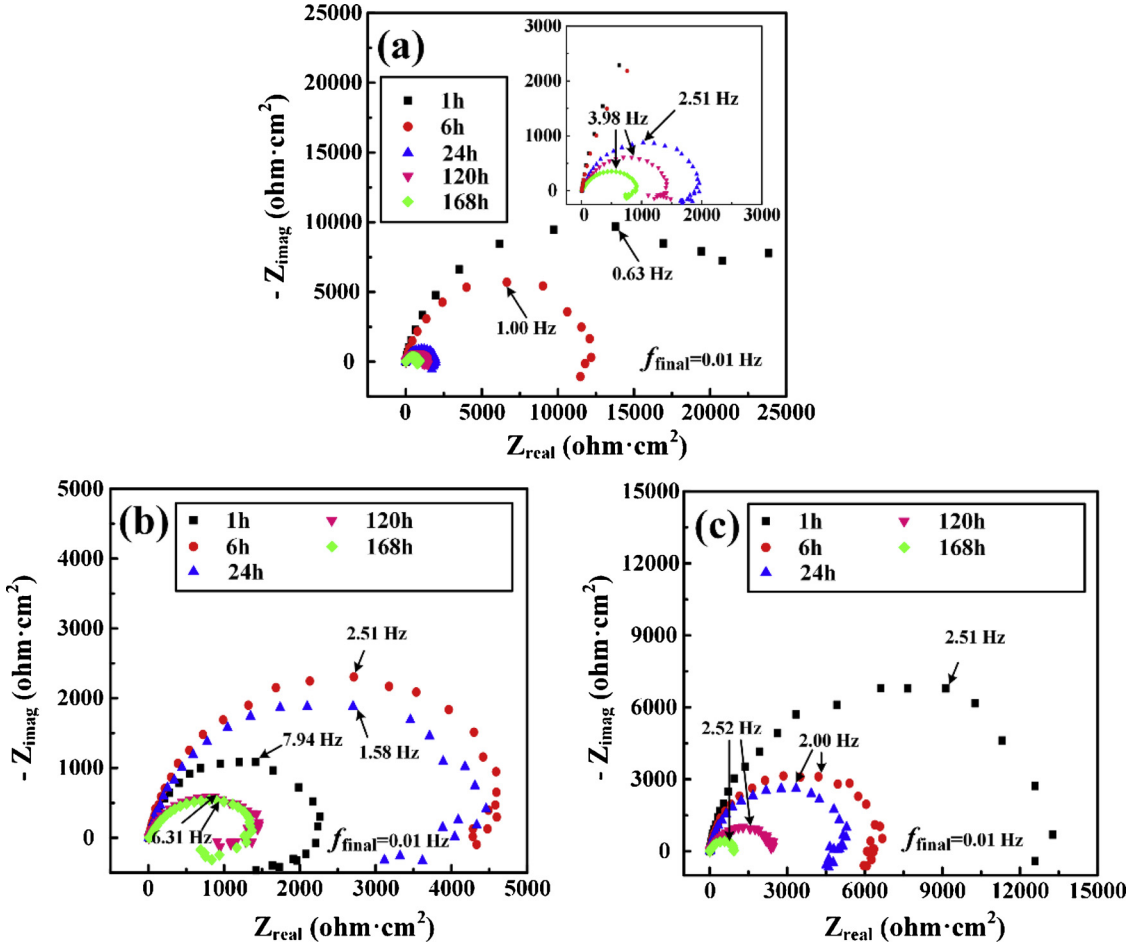

Fig. 6. EIS plots of (a) 6061, (b) 0.5-TiC_p and (c) 0.5-TiB_{2p} in 3.5 wt% NaCl solution (19.6 ± 0.2 °C, pH 7.3 ± 0.5).

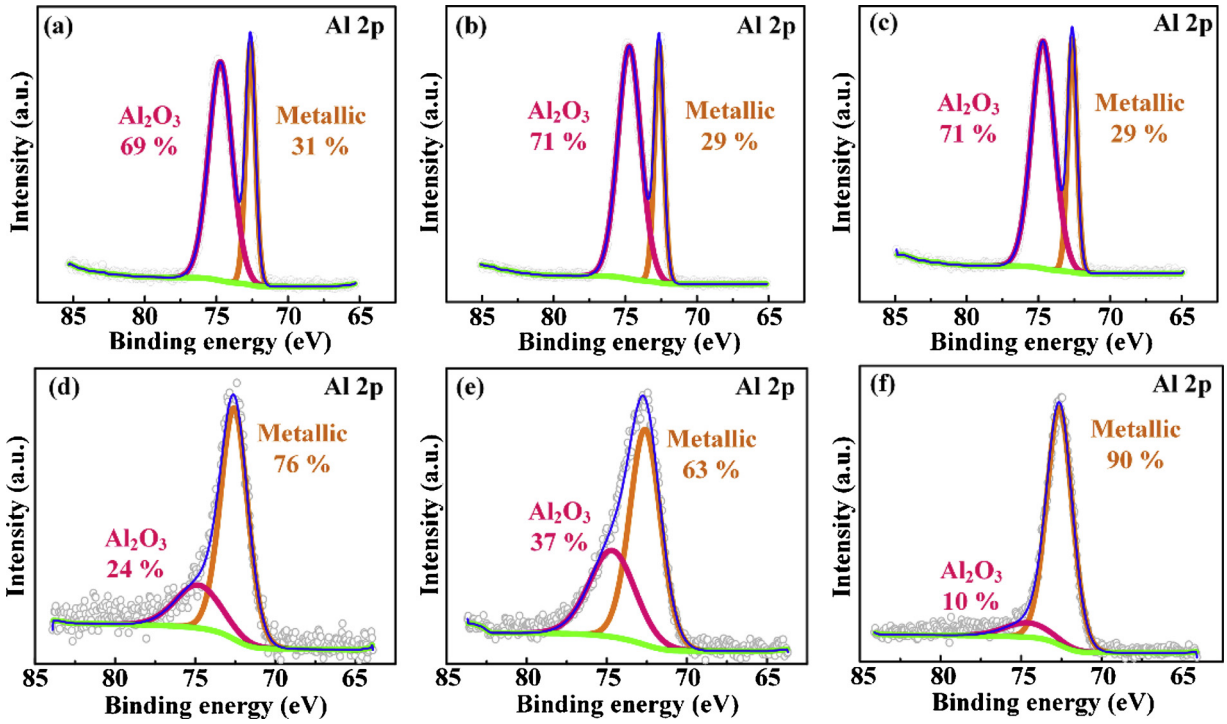

Fig. 7. Al 2p XPS peaks of the sample surfaces before the corrosion test: (a) the matrix alloy, (b) the 0.5-TiC_p composite and (c) the 0.5-TiB_{2p} composite; Peaks obtained after the accelerated corrosion test: (d) the matrix alloy, (e) the 0.5-TiC_p composite and (f) the 0.5-TiB_{2p} composite.

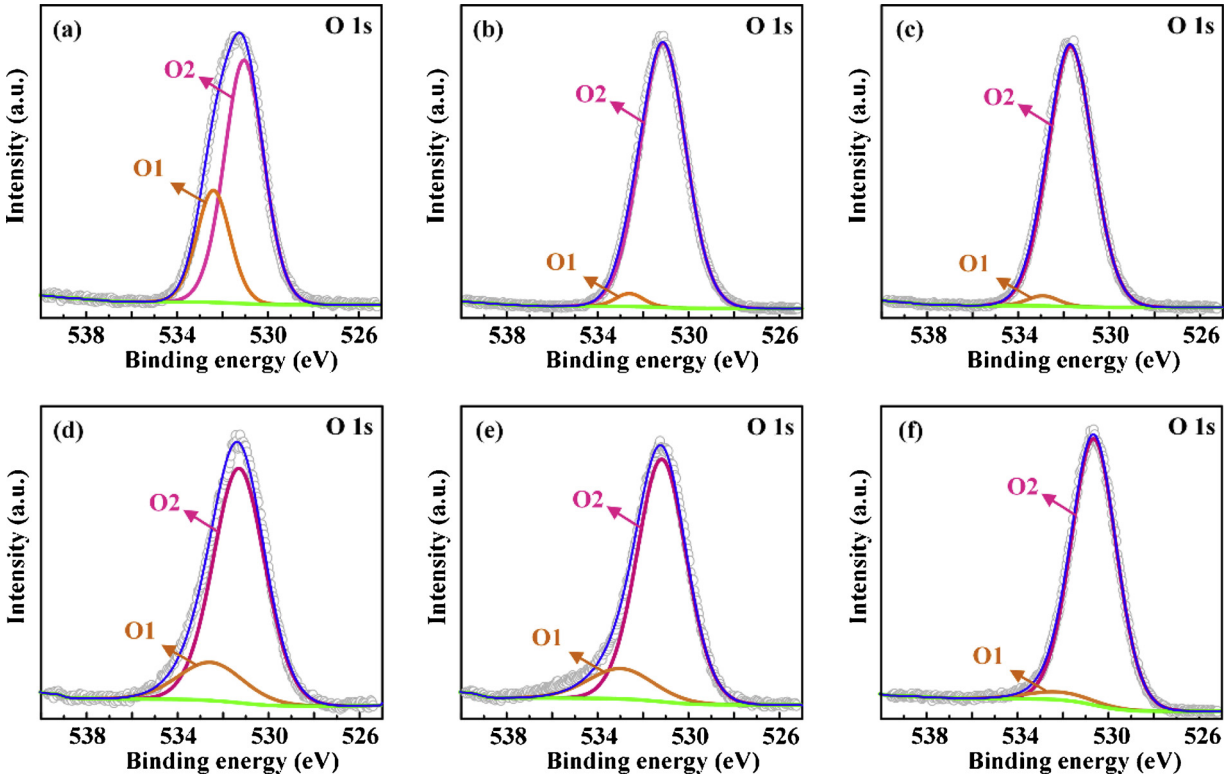

Fig. 8. O 1s XPS peaks of the sample surfaces before the corrosion test: (a) the matrix alloy, (b) the 0.5-TiC_p composite and (c) the 0.5-TiB_{2p} composite; Peaks obtained after the accelerated corrosion test: (d) the matrix alloy, (e) the 0.5-TiC_p composite and (f) the 0.5-TiB_{2p} composite. Two characteristic peaks of surface-adsorbed oxygen (O1) and oxygen in Al_2O_3 (O2).

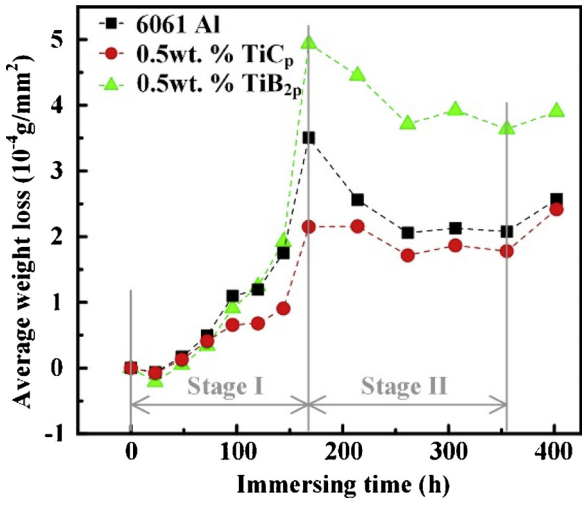

Fig. 9. Average weight loss of the matrix alloy and the composites with different nanoparticles in the 3.5 wt% NaCl solution.

of these materials possessed a similar content of Al_2O_3 before the accelerated corrosion test (~ 70 %). The remaining Al_2O_3 was a key factor in ensuring corrosion resistance. For the samples after the accelerated corrosion test, the contents of the Al_2O_3 were 38 %, 24 % and 10 % in the 0.5-TiC_p composite, the matrix alloy, and the 0.5-TiB_{2p} composite, respectively. This result is consistent with the MCD result in the accelerated corrosion test (Fig. 3). The XPS results indicated that the uniformity of the passivation was the best in the 0.5-TiC_p composite and the worst in the 0.5-TiB_{2p} composite.

3.1.4. Immersing corrosion tests

These materials were immersed in the 3.5 wt% NaCl solution to investigate the corrosion process. The average corrosion weight losses of the matrix alloy and the composites with different nanoparticles are shown in Fig. 9. The average corrosion weight loss of these materials increased with time until 168 h and then decreased until 355 h. Fig. 10 shows the photographs of the matrix alloy, the 0.5-TiC_p composite and the 0.5-TiB_{2p} composite before and after immersing for 402 h in the 3.5 wt% NaCl solution. In the 3.5 wt% NaCl solution, some deeper corrosion holes with a larger area indicated a severe IGC compared with uniform corrosion occurrence (Fig. 4) [29]. The area fraction of the severe corrosion regions was the largest in the 0.5-TiB_{2p} composite and the smallest in the 0.5-TiC_p composite, indicating that the corrosion behavior of 0.5-TiC_p composite improved as compared to the matrix alloy and the 0.5-TiB_{2p} composite. This was in accordance with the accelerating corrosion results (Fig. 4). The corrosion holes were shallow and the corrosion area decreases in the 0.5-TiC_p composite.

The entire corrosion process can be divided into two stages. Stage I is from the beginning of the test to 168 h, and stage II is from 168 h to 355 h. Stages I and II together can be seen as a corrosion cycle. The Al_2O_3 film generated on the surface is a key factor to improve the corrosion resistance. However, the Al_2O_3 film is generally non-uniform, thin and no-coherent. The grain boundary phases can cause the IGC cracks, further resulting in the weight losses during the immersing corrosion test [30]. In stage I, the Al_2O_3 film was generated and consumed with the occurrence of pitting corrosion and IGC (Fig. 4). During the corrosion process, the IGC cracks can cause the exfoliation corrosion, leading to severe weight losses at the peak of stage I, as shown in Fig. 9. In stage II, the new Al_2O_3 film was regenerated, and thus, the slope of weight loss decreased. This was the beginning of the next corrosion cycle after 355 h. The decrease in stage II of the 0.5-TiC_p composite was the least, indicating that the exfoliation corrosion in the 0.5-TiC_p composite was the weakest.

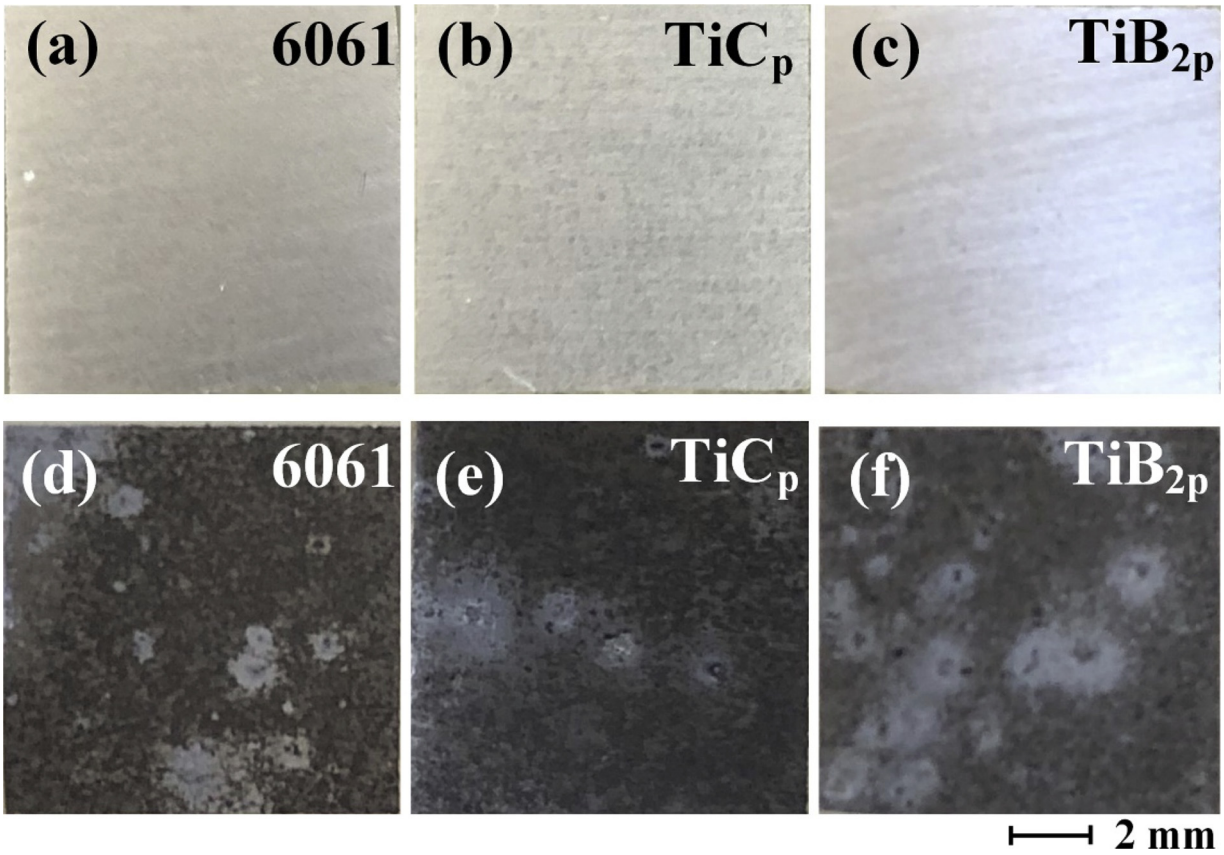

Fig. 10. Photographs of (a) the matrix alloy, (b) the 0.5-TiC_p composite and (c) the 0.5-TiB_{2p} composite after polishing; (d)-(f) are the photographs of the matrix alloy, the 0.5-TiC_p composite, and the 0.5-TiB_{2p} composite after immersing in 3.5 wt% NaCl solution for 402 h.

3.2. Microstructures

3.2.1. Grain microstructures

Fig. 11(a–c) show the grain microstructures of the matrix alloy, the 0.5-TiC_p composite, and the 0.5-TiB_{2p} composite. The mean grain sizes in the 0.5-TiC_p and 0.5-TiB_{2p} composites were refined from 69 μm to 20 μm, and the refined grain structures were beneficial for improving the corrosion behaviors [19]. The matrix alloy possessed a broader grain size distribution as compared to the 0.5-TiC_p composite and the 0.5-TiB_{2p} composite (Fig. 11(d–f)), with 80 % of the grain sizes distributed below 105 μm, 25 μm and 25 μm in the matrix alloy, the 0.5-TiC_p composite, and the 0.5-TiB_{2p} composite, respectively.

3.2.2. TEM

The grain boundary phases distributed discontinuously in the matrix alloy (Fig. 12 (a)). Few grain boundary phases were found in the 0.5-TiC composite (Fig. 12(b)). The grain boundary phases were distributed densely in the 0.5-TiB_{2p} composite (Fig. 12(c)). Fig. 12(d–f) show the statistical results of the dispersion distance (D_d) between the adjacent grain boundary second phases in these samples. The D_d and the number of the grain boundary second phases were measured via TEM images. The results were obtained by observing 20 pictures with the same magnification of the grain boundary regions in each material. The numbers of the grain boundary second phases in the matrix alloy, the 0.5-TiC_p composite, and the 0.5-TiB_{2p} composite were 193, 103 and 226, respectively. The average dispersion distances ($\bar{D}_d$) between the adjacent grain boundary second phases in the matrix alloy, the 0.5-TiC_p composite, and the 0.5-TiB_{2p} composite were 396 nm, 780 nm, and 382 nm, respectively. As shown in Fig. 13(a), the main phases at the grain boundaries were AlFeSi dispersoids, Mg_2Si and excess Si in the 0.5-TiC_p composite. Except for the AlFeSi dispersoids, the Mg_2Si and the excess Si, there was some TiB_{2p} at the grain boundaries in the 0.5-TiB_{2p} composite (Fig. 13(b)). This indicated that the extra grain boundary phases in the 0.5-TiB_{2p} composite were caused by the segregation of TiB_{2p} at the grain boundaries, compared to the matrix alloy and the 0.5-TiC_p composite. Thus, the IGC susceptibilities of these materials related to the different number of grain boundary phases.

4. Discussion

As shown in Fig. 14(a), the TiC possesses a fcc crystal structure. The shape of TiC_p is spherical in this work, and the (111) and (100) surfaces are obtained as mentioned in our previous work [31]. Based on the cube to cube orientation relation, $(111)_{TiC}//(111)_{Al}$ and $(100)_{TiC}//(100)_{Al}$ possess a low mismatch (6.9 %). Thus, the TiC_p can act as heterogeneous nucleation sites of α-Al during solidification to refine the grain structure and distribute inside the grains (Fig. 15(a)). As shown in Fig. 14(b), the TiB_2 possesses an hcp crystal structure, and the shape of TiB_{2p} is a hexahedron that possesses many surfaces in this work. Only $(0001)_{TiB2}//(111)_{Al}$ has a low mismatch (5.8 %). although TiB_{2p} can act as the heterogeneous nucleation sites of α-Al, most of them were distributed at grain boundaries (Fig. 15(b)). Some of the TiB_{2p} can act as the heterogeneous nucleation cores of α-Al during solidification to refine the grain structure. However, the TiB_{2p} that distributed at the grain boundaries could resist the movement of the grain boundaries and impede grain growth during the recrystallization process [6]. As a result, the average grain sizes in the 0.5-TiC_p composite and the 0.5-TiB_{2p} composite were similar, but the distributions of TiC_p and TiB_{2p} are different. The TiB_{2p} at grain boundaries led to an increasing number of the grain boundary second phases (grain boundary particles) in the 0.5-TiB_{2p} composite. These grain boundary particles would form micro galvanic couplings to accelerate the IGC.

The segregation of Mg and Si would form some Mg_2Si and excess Si at the grain boundaries (Fig. 13). However, the refined grain structures

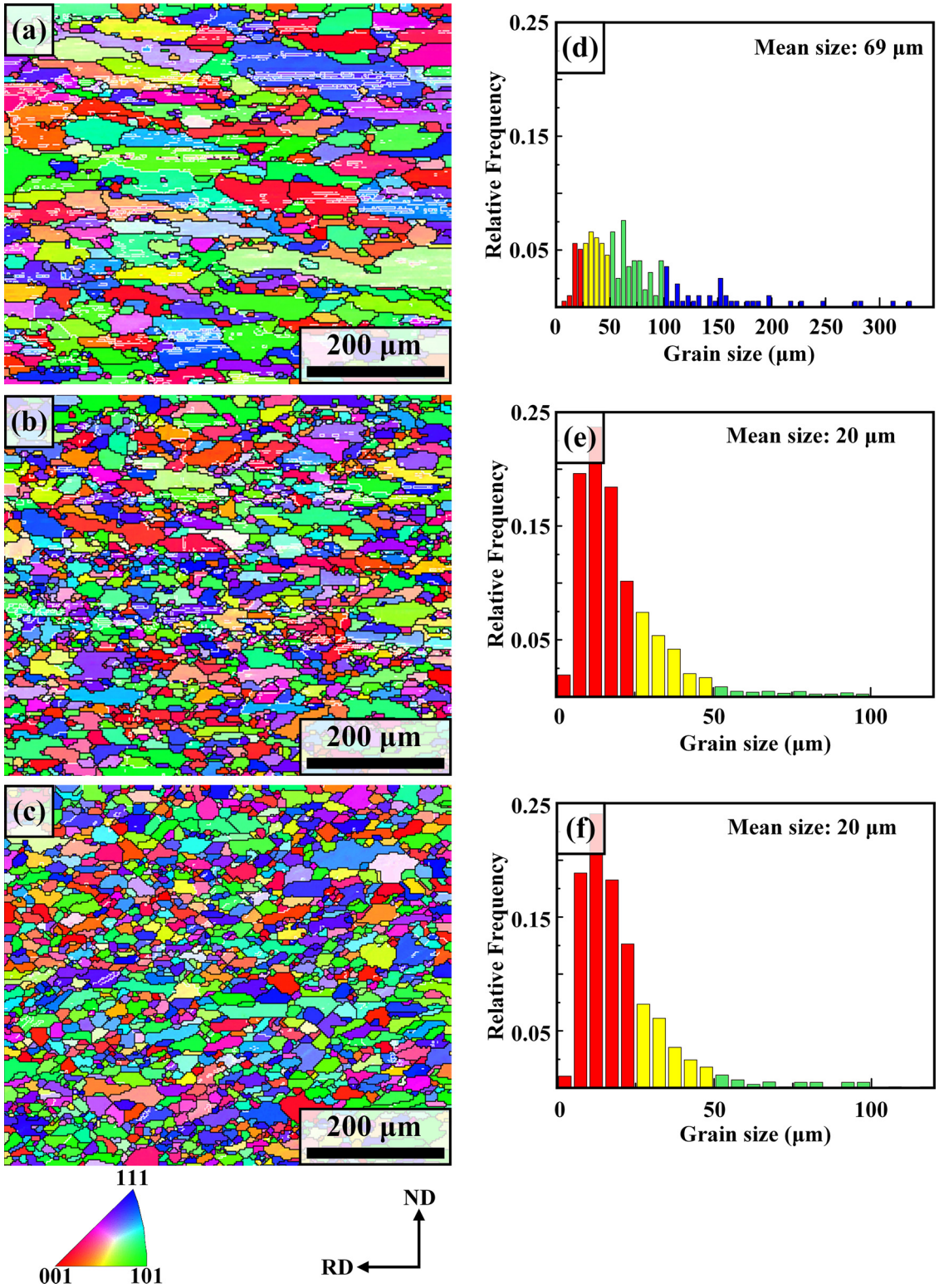

Fig. 11. EBSD images of (a) the matrix alloy, (b) the 0.5-TiC_p composite and (c) the 0.5-TiB_{2p} composite, and (d–f) the corresponding grain size distribution.

of the 0.5-TiC_p composite could increase the total area of the grain boundaries and reduce the diffusion distance of the solid solution elements during the solution treatment. As a result, the refined grain structure promoted a better solution effect, leading to the reduction of the grain boundary (Mg_2Si and excess Si) [9]. The refined grain structure provided a relatively discrete distribution of these dispersoids at the grain boundaries, thus reducing the number of corrosion channels, compared to the matrix alloy. Thus, the number density of grain boundary second phases was reduced, and the refined and uniform grains could cause a more obvious passivity effect in the 0.5-TiC_p composite, compared to the matrix alloy.

The refined grain structure of the 0.5-TiB_{2p} composite was also beneficial for the reduction of Mg_2Si, AlFeSi dispersoids and excess Si at the grain boundaries, compared to the matrix alloy. As discussed above,

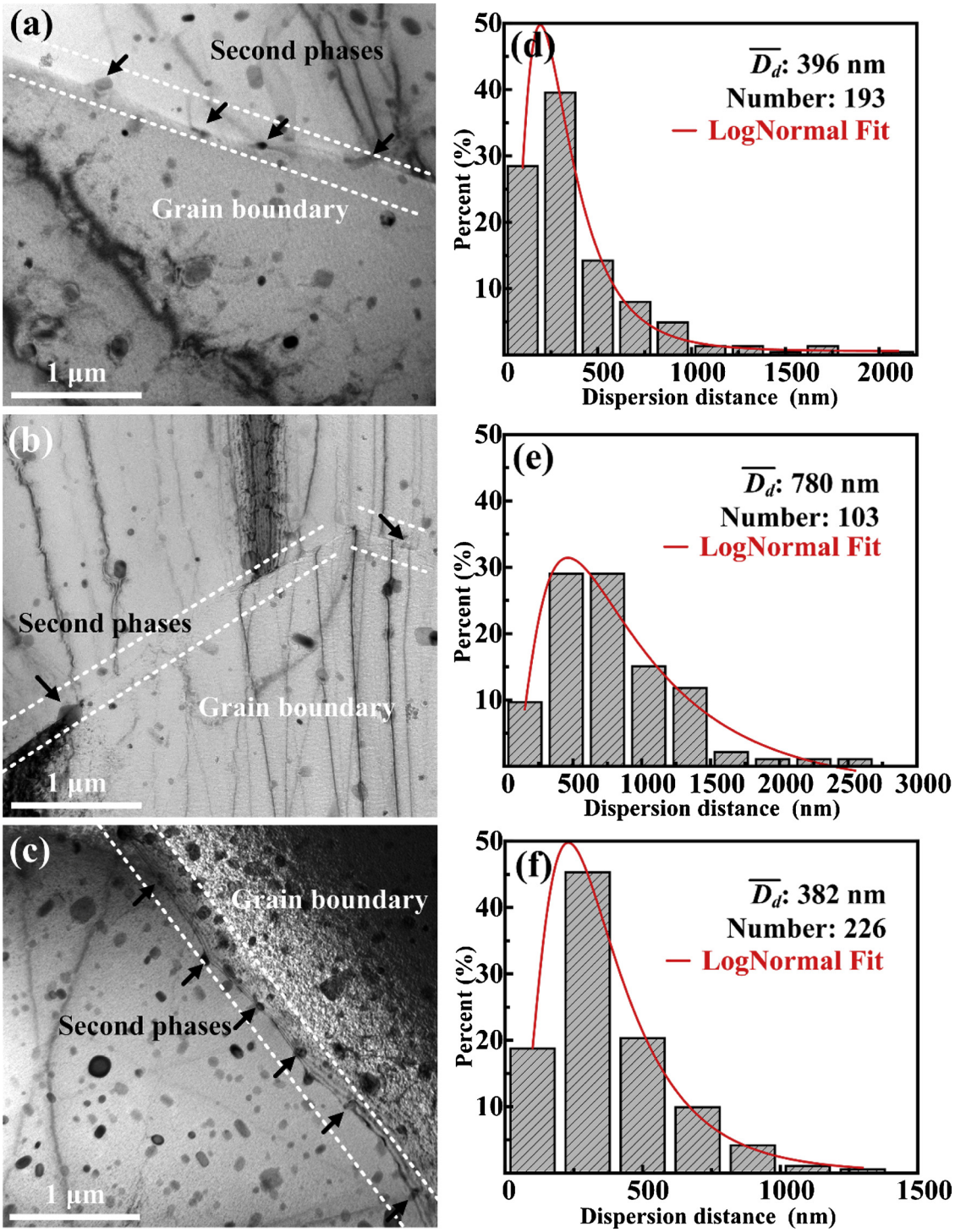

Fig. 12. TEM micrographs of (a) the matrix alloy, (b) the 0.5-TiC_p composite and (c) the 0.5-TiB_{2p} composite. The statistical results of the dispersion distance (D_d) of the second phase at the grain boundaries are shown for (d) the matrix alloy, (e) the 0.5-TiC_p composite and (f) the 0.5-TiB_{2p} composite.

most of the TiB_{2p} segregated at the grain boundaries, leading to an increased number of grain boundary particles, compared to the 0.5-TiC_p composite. As a result, the passivity was weakened, and the corrosion rate increased in the 0.5-TiB_{2p} composite.

In a passivating environment, the passive film (the Al_2O_3 film in this paper) on the corrosion surfaces will be more uniform if the grain size distribution is more narrow [23]. However, the denser grain boundary second phases in the 0.5-TiB_{2p} composite increased the IGC rate and caused the worse corrosion performance, compared to the matrix alloy and the 0.5-TiC_p composite.

In general, the refined and uniformed grain structures caused by the addition of the nanoparticles had a significant passivity effect [19]. However, the micro galvanic couplings formed by the grain boundary second phases led to severe IGC. At the beginning of stage I, the Al_2O_3 film formed in these alloys impeded the pitting corrosion and IGC. During stage I, the exfoliation corrosion was resulted by the IGC cracks. However, the IGC rate and the uniformity of the Al_2O_3 film in these alloys were different. The Al_2O_3 film of the matrix alloy was not uniform because of the coarse and uneven grain structure [23]. During the immersion in NaCl solution, there were no continuous and compact

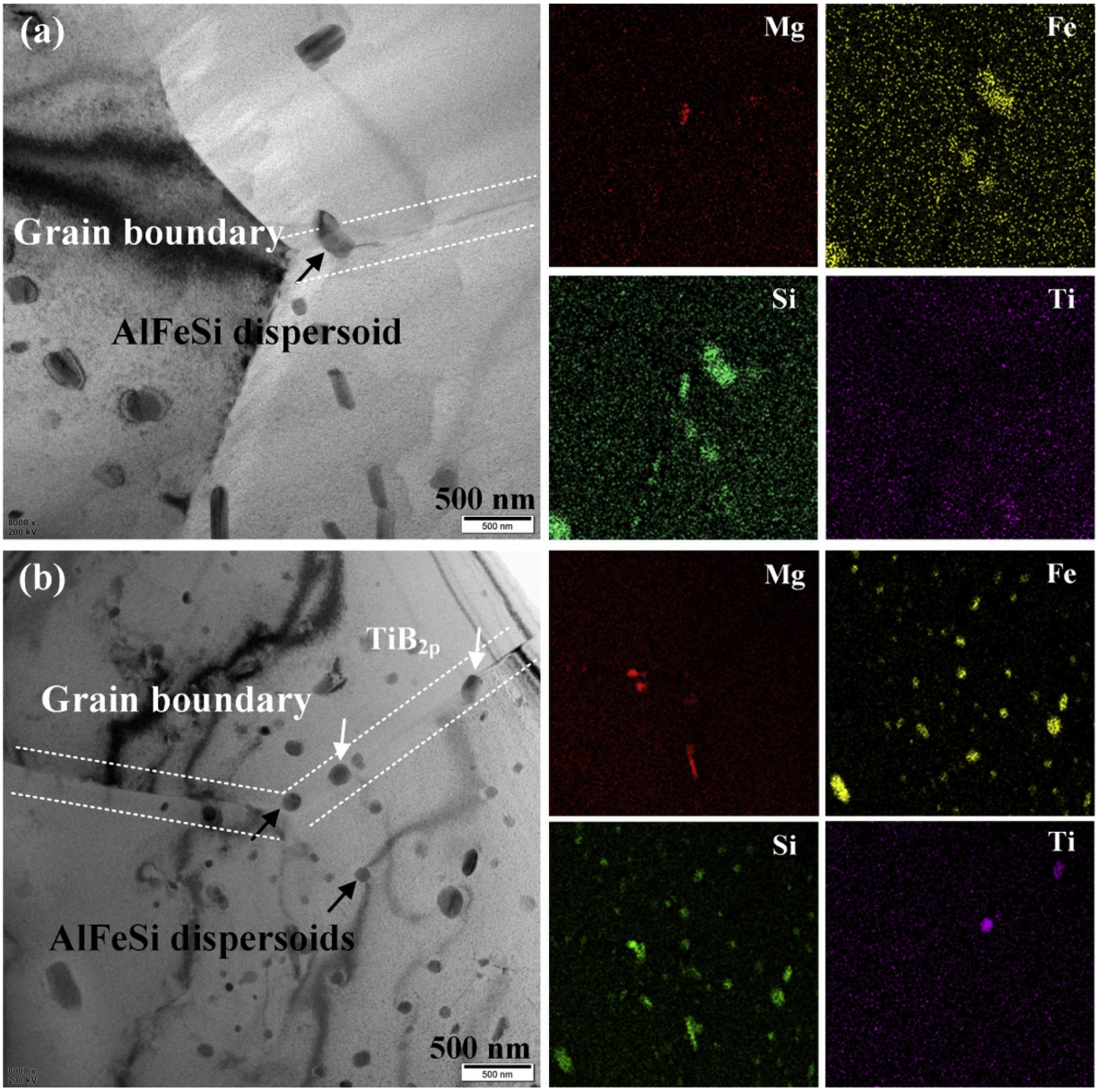

Fig. 13. TEM micrographs and corresponding EDS results of the grain boundaries in (a) the 0.5-TiC_p composite and (b) the 0.5-TiB_{2p} composite.

protective Al_2O_3 around its grain boundaries. Hence, severe IGC happened with the degradation of corrosion resistance (Fig. 6(a)), further leading to the exfoliation corrosion and the severe weight losses during stage I. The 0.5-TiC_p composite contained less grain boundary second phases, and the refined and uniform grains could cause a more obvious passivity effect. The reduced number of grain boundary second phases slowed the IGC rate, compared to the matrix alloy. Thus, the 0.5-TiC_p composite showed improved corrosion resistance in stage I, compared to the matrix alloy (Fig. 6(b)). The refined and uniform grain structure of the 0.5-TiB_{2p} composite could also cause a passivity effect as shown in Fig. 5, compared to the matrix alloy. However, the TiB_{2p} distributed at the grain boundaries, leading to a higher IGC rate. As a result, the corrosion rate increased in 0.5-TiB_{2p} composite (Fig. 6(c)). The denser grain boundary second phases in the 0.5-TiB_{2p} composite broke up the uniformity of the Al_2O_3 film during formation, leading to the discontinuity of the generated Al_2O_3 film. The grain boundary second phases were distributed sparsely in the 0.5-TiC_p composite, causing the uniformity of the passive film to be retained and decreasing the IGC rate. As a result, the degradation of corrosion resistance and higher IGC rate together caused the higher slope of the weight-loss curves in the matrix alloy and the 0.5-TiB_{2p} composite, compared to the 0.5-TiC_p composite. In stage II, the new generation of Al_2O_3 film impeded the corrosion process, further leading to the decreasing slope of weight loss. However, the corrosion surface became larger during the exfoliation corrosion, and the 0.5-TiB_{2p} composite showed the most severe exfoliation corrosion because of the higher IGC rate as mentioned above (Fig. 3). The 0.5-TiB_{2p} composite showed a deep network-sharped IGC with severe exfoliation corrosion, while the IGC was impeded in the 0.5-TiC_p composite (Fig. 3). Thus, the weight loss of the 0.5-TiB_{2p} composite in stage II was the highest (Figs. 3(c) and 9). The contents of the Al_2O_3 detected by the XPS measurements were 24 %, 37 % and 10 % in the matrix alloy, the 0.5-TiC_p composite, and the 0.5-TiB_{2p} composite, respectively. The protective effect of the Al_2O_3 film improved the pitting corrosion and the reduced number of grain boundary second phases improved the IGC. Therefore, the improved corrosion behaviors were observed in the 0.5-TiC_p composite.

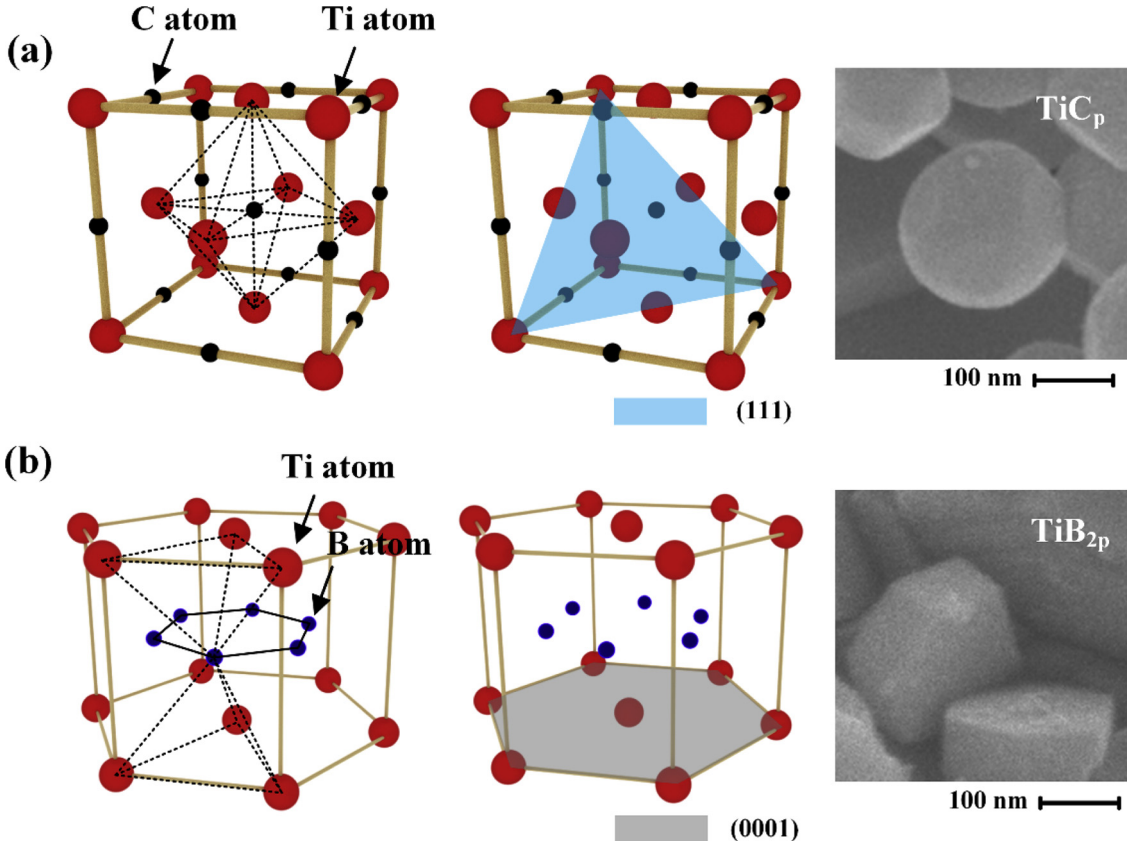

Fig. 14. The crystal structure diagrams and morphologies of the (a) TiC and (b) TiB_2.

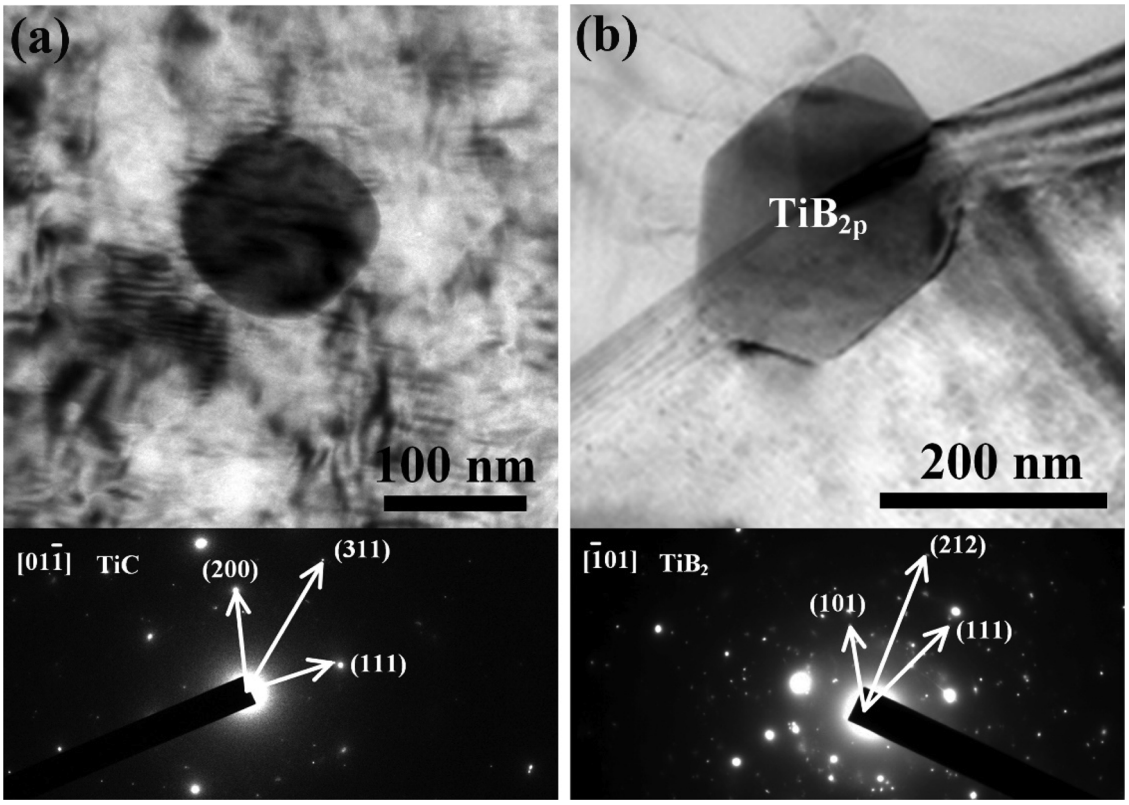

Fig. 15. (a) The TiC_p inside the grain and (b) the TiB_{2p} distributed at the grain boundary.

5. Conclusions

In this work, the corrosion behavior of an Al-Mg-Si alloy was investigated after the addition of different nanoparticles. The following conclusions are drawn:

I The corrosion behavior of the Al-Mg-Si alloy was improved by adding nanosized TiC_p, while it worsened after adding nanosized TiB_{2p} in both the accelerated corrosion solution and the 3.5 wt% NaCl solution.

II The nanosized TiC_p and TiB_{2p} can both refine the grain structure of the matrix Al alloy. The nanosized TiC_p distributed mostly inside the grains refined the grain structure by acting as nucleants. The nanosized TiB_{2p} distributed mostly at the grain boundaries and increased grain boundary particles. The refined grain structure was beneficial for the diffusion of the solution elements (Mg/Si) during the solution treatment, thus reducing the amount of Mg_2Si and excess Si at grain boundaries after the aging process. The nanosized TiC_p reduced the number of grain boundary second phases, leading to a reduced corrosion rate. The nanosized TiB_{2p} caused denser grain boundary second phases, increasing the corrosion rate.

III A criterion for the selection of reinforcement nanoparticles in wrought aluminum alloys was also proposed. The segregation of nanoparticles on grain boundaries decreases the corrosion resistance of wrought aluminum alloys. The distribution of particles depends on the crystal structure of the nanoparticles and the interface mismatch. Nanosized TiC_p are more capable of distributing inside the Al grains as compared to nanosized TiB_{2p}, because the nanosized TiC_p have more low-mismatch interfaces with α-Al.

Data availability statement

The raw/processed data required to reproduce these findings cannot be shared at this time as the data also forms part of an ongoing study.

CRediT authorship contribution statement

Run Geng: Validation, Formal analysis, Investigation, Writing - original draft, Visualization. **Si-Qi Jia:** Software, Data curation. **Feng Qiu:** Resources. **Qing-Long Zhao:** Writing - review & editing, Project administration. **Qi-Chuan Jiang:** Conceptualization, Methodology, Supervision, Funding acquisition.

Declaration of Competing Interest

The authors declared that they have no conflicts of interest to this work.

We declare that we do not have any commercial or associative interest that represents a conflict of interest in connection with the work submitted.

Acknowledgments

This work was funded by the National Natural Science Foundation of China (Grant Nos. 51790483 and 51571101) and the Science and Technology Development Program of Jilin Province, China (Grant No. 20170101215JC).

Appendix A. Supplementary data

Supplementary material related to this article can be found, in the online version, at doi:https://doi.org/10.1016/j.corsci.2020.108479.

References

[1] B.T. Sofyan, D.J. Kharistal, L. Trijati, K. Purba, R.E. Susanto, Grain refinement of AA333 aluminium cast alloy by Al–Ti granulated flux, Mater. Des. 31 (2010) S36–S43, https://doi.org/10.1016/j.matdes.2010.02.007.

[2] G.S.V. Kumar, B.S. Murty, M. Chakraborty, Grain refinement response of LM25 alloy towards Al–Ti–C and Al–Ti–B grain refiners, J. Alloys Compd. 472 (2009) 112–120, https://doi.org/10.1016/j.jallcom.2008.04.095.

[3] Z. Fan, Y. Wang, Y. Zhang, T. Qin, X.R. Zhou, G.E. Thompson, T. Pennycook, T. Hashimoto, Grain refining mechanism in the Al/Al–Ti–B system, Acta Mater. 84 (2015) 292–304, https://doi.org/10.1016/j.actamat.2014.10.055.

[4] W.S. Tian, Q.L. Zhao, Q.Q. Zhang, F. Qiu, Q.C. Jiang, Enhanced strength and ductility at room and elevated temperatures of Al-Cu alloy matrix composites reinforced with bimodal-sized TiCp compared with monomodal–sized TiCp, Mater. Sci. Eng. A. 724 (2018) 368–375, https://doi.org/10.1016/j.msea.2018.03.106.

[5] R. Geng, F. Qiu, Q.L. Zhao, Y.Y. Gao, Q.C. Jiang, Effects of nanosized TiCp on the microstructure evolution and tensile properties of an Al-Mg-Si alloy during cold rolling, Mater. Sci. Eng. A. 743 (2019) 98–105, https://doi.org/10.1016/j.msea.2018.11.078.

[6] L. Wang, F. Qiu, Q. Zhao, M. Zha, Q. Jiang, Superior high creep resistance of in situ nano-sized TiCx/Al-Cu-Mg composite, Sci. Rep. 7 (2017) 1–10, https://doi.org/10.1038/s41598-017-04816-0.

[7] W.S. Tian, Q.L. Zhao, Q.Q. Zhang, F. Qiu, Q.C. Jiang, Superior creep resistance of 0.3 wt% nano-sized TiCp/Al-Cu composite, Mater. Sci. Eng. A 700 (2017) 42–48, https://doi.org/10.1016/j.msea.2017.05.101.

[8] W.S. Tian, Q.L. Zhao, C.J. Zhao, F. Qiu, Q.C. Jiang, The dry sliding wear properties of nano-sized TiCp/Al-Cu composites at elevated temperatures, Materials (Basel) 10 (2017) 939, https://doi.org/10.3390/ma10080939.

[9] W.S. Tian, D.S. Zhou, F. Qiu, Q.C. Jiang, Superior tensile properties of in situ nano-sized TiCp/Al-Cu composites fabricated by reaction in melt method, Mater. Sci. Eng. A 658 (2016) 409–414, https://doi.org/10.1016/j.msea.2016.02.015.

[10] J.M.G. De Salazar, A. Urena, S. Manzanedo, M.I. Barrena, Corrosion behaviour of AA6061 and AA7005 reinforced with Al2O3 particles in aerated 3.5% chloride solutions: potentiodynamic measurements and microstructure evaluation, Corros. Sci. 41 (1999) 529–545.

[11] Y. Zou, Q. Liu, Z. Jia, Y. Xing, L. Ding, X. Wang, The intergranular corrosion behavior of 6000-series alloys with different Mg/Si and Cu content, Appl. Surf. Sci. 405 (2017) 489–496, https://doi.org/10.1016/j.apsusc.2017.02.045.

[12] V. Guillaumin, G. Mankowski, Localized corrosion of 6056 T6 aluminium alloy in chloride media, Corros. Sci. 42 (2000) 105–125, https://doi.org/10.1016/S0010-938X(99)00053-0.

[13] T.D. Burleigh, E. Ludwiczak, R.A. Petri, Intergranular corrosion of an aluminum-magnesium-silicon-copper alloy, Corrosion 51 (1995) 50–55, https://doi.org/10.5006/1.3293577.

[14] X. Zhang, X. Zhou, J.-O. Nilsson, Z. Dong, C. Cai, Corrosion behaviour of AA6082 Al-Mg-Si alloy extrusion: recrystallized and non-recrystallized structures, Corros. Sci. 144 (2018) 163–171, https://doi.org/10.1016/j.corsci.2018.08.047.

[15] N.C.W. Kuijpers, F.J. Vermolen, C. Vuik, P.T.G. Koenis, K.E. Nilsen, S. van der Zwaag, The dependence of the β-AlFeSi to α-Al(FeMn)Si transformation kinetics in Al-Mg-Si alloys on the alloying elements, Mater. Sci. Eng. A 394 (2005) 9–19, https://doi.org/10.1016/j.msea.2004.09.073.

[16] M.S. Remøe, K. Marthinsen, I. Westermann, K. Pedersen, J. Røyset, C. Marioara, The effect of alloying elements on the ductility of Al-Mg-Si alloys, Mater. Sci. Eng. A 693 (2017) 60–72, https://doi.org/10.1016/j.msea.2017.03.078.

[17] D. Chakrabarti, D.E. Laughlin, Phase relations and precipitation in Al-Mg-Si alloys with Cu additions, Prog. Mater. Sci. 49 (2004) 389–410, https://doi.org/10.1016/S0079-6425(03)00031-8.

[18] Q. Li, F. Qiu, B. Dong, R. Geng, M. Lv, Q. Zhao, Q.-C. Jiang, Fabrication, microstructure refinement and strengthening mechanisms of nanosized SiCp/Al composites assisted ultrasonic vibration, Mater. Sci. Eng. A 735 (2018) 310–317, https://doi.org/10.1016/j.msea.2018.08.060.

[19] K.D. Ralston, N. Birbilis, Effect of grain size on corrosion: a review, Corrosion 66 (2010) 0750051–07500513, https://doi.org/10.5006/1.3462912.

[20] M.K. Chung, Y.S. Choi, J.G. Kim, Y.M. Kim, J.C. Lee, Effect of the number of ECAP pass time on the electrochemical properties of 1050 Al alloys, Mater. Sci. Eng. A 366 (2004) 282–291, https://doi.org/10.1016/j.msea.2003.08.056.

[21] T.C. Tsai, T.H. Chuang, Role of grain size on the stress corrosion cracking of 7475 aluminum alloys, Mater. Sci. Eng. A 225 (1997) 135–144, https://doi.org/10.1016/S0921-5093(96)10840-6.

[22] D. SONG, Ab. MA, Jh. JIANG, Ph. LIN, Dh. YANG, Corrosion behavior of ultra-fine grained industrial pure Al fabricated by ECAP, Trans. Nonferrous Met. Soc. China 19 (2009) 1065–1070, https://doi.org/10.1016/S1003-6326(08)60407-0 English Ed..

[23] S. Gollapudi, Grain size distribution effects on the corrosion behaviour of materials, Corros. Sci. 62 (2012) 90–94, https://doi.org/10.1016/j.corsci.2012.04.040.

[24] J. lei Huang, J. feng Li, D. yang Liu, R. feng Zhang, Y. lai Chen, X. hu Zhang, P. cheng Ma, R.K. Gupta, N. Birbilis, Correlation of intergranular corrosion behaviour with microstructure in Al-Cu-Li alloy, Corros. Sci. 139 (2018) 215–226, https://doi.org/10.1016/j.corsci.2018.05.011.

[25] Z. Wang, F. Zhu, K. Zheng, J. Jia, Y. Wei, H. Li, L. Huang, Z. Zheng, Effect of the thickness reduction on intergranular corrosion in an under–aged Al–Mg–Si–Cu alloy during cold–rolling, Corros. Sci. 142 (2018) 201–212, https://doi.org/10.1016/j.corsci.2018.07.018.

[26] H. lan Wu, Y. liang Cheng, L. ling Li, Z. hua Chen, H. min Wang, Z. Zhang, The anodization of ZK60 magnesium alloy in alkaline solution containing silicate and the corrosion properties of the anodized films, Appl. Surf. Sci. 253 (2007) 9387–9394, https://doi.org/10.1016/j.apsusc.2007.05.085.

[27] N. Saleema, D.K. Sarkar, R.W. Paynter, D. Gallant, M. Eskandarian, A simple surface treatment and characterization of AA 6061 aluminum alloy surface for adhesive

bonding applications, Appl. Surf. Sci. 261 (2012) 742–748, https://doi.org/10.1016/j.apsusc.2012.08.091.
[28] Q. Zhang, N.M. Bedford, J. Pan, X. Lu, R. Amal, A Fully Reversible Water Electrolyzer Cell Made Up from FeCoNi (Oxy)hydroxide Atomic Layers, Adv. Energy Mater. 9 (2019) 1901312,, , https://doi.org/10.1002/aenm.201901312.
[29] Z. Bai, Y. Xia, F. Qiu, Y. Liu, W. Hu, Q. Jiang, Effects of RExOy addition on corrosion behavior of the Al–Cu alloys in 3.5wt.% NaCl solution and pH = 4 acid solution, Appl. Surf. Sci. 307 (2014) 153–157, https://doi.org/10.1016/j.apsusc.2014.03.198.
[30] W.G. Zhao, J.G. Wang, H.L. Zhao, J.Q. Hou, Q.C. Jiang, Corrosion mechanism of the modified casting Al–Cu alloy by the nano-scale PrxOy, J. Alloys Compd. 479 (2009) L30–L35, https://doi.org/10.1016/j.jallcom.2008.12.095.
[31] S.B. Jin, P. Shen, Q.L. Lin, L. Zhan, Q.C. Jiang, Growth mechanism of TiCx during self-propagating high-temperature synthesis in an Al − Ti − C system, Cryst. Growth Des. 10 (2010) 1590–1597, https://doi.org/10.1021/cg9010983.